A Coupled Ocean–Atmosphere Instability of Relevance to the Seasonal Cycle

PING CHANG

Department of Oceanography, Texas A&M University, College Station, Texas

S. GEORGE PHILANDER

Atmospheric and Oceanic Science Program, Princeton University, Princeton, New Jersey

(Manuscript received 13 September 1993, in final form 11 May 1994)

ABSTRACT

Recent observational studies have suggested that interactions between the atmosphere and the ocean play an important role in the pronounced annual cycle of the eastern equatorial Pacific and Atlantic Oceans. The key to this atmosphere–ocean interaction is a positive feedback between the surface winds and the local SST gradients in the cold tongue/ITCZ complex regions, which leads to an instability in the coupled system. By means of linear instability analyses and numerical model experiments, such an instability mechanism is explored in a simple coupled ocean–atmosphere system. The instability analysis yields a family of antisymmetric and symmetric unstable SST modes. The antisymmetric mode has the most rapid growth rate. The most unstable antisymmetric mode occurs at zero wavenumber and has zero frequency. The symmetric SST mode, although its growth rate is smaller, has a structure at annual period that appears to resemble the observed westward propagating feature in the annual cycle of near-equatorial zonal wind and SST. Unlike the ENSO type of coupled unstable modes, the modes of relevance to the seasonal cycle do not involve changes in the thermocline depth. The growth rates of these modes are linearly proportional to the mean vertical temperature gradient and inversely proportional to the depth of mean thermocline in the ocean. Because of the shallow thermocline and strong subsurface thermal gradients in the eastern Pacific and Atlantic Oceans, these coupled unstable modes strongly influence the seasonal cycles of those regions. On the basis of theoretical analyses and the observational evidence, it is suggested that the antisymmetric SST mode may be instrumental in rapidly reestablishing the cold tongues in the eastern Pacific and Atlantic Oceans during the Northern Hemisphere summer, whereas the symmetric SST mode contributes to the westward propagating feature in the annual cycle of near-equatorial zonal winds and SST.

1. Introduction

The seasonal cycle, the forced response of the earth's climate to the periodic change in the solar radiation, involves complex interactions between the atmosphere, ocean, and the land surfaces. These interactions manifest themselves in the distinctive character of the seasonal cycle in different parts of the globe. For example, in the Tropics, climate conditions have striking asymmetries relative to the equator in the Atlantic and eastern Pacific but are essentially symmetrical about the equator elsewhere. These asymmetries characterize time-mean conditions and also the seasonal cycle. Their distinguishing features include sea surface temperature maxima to the north of the equator, atmospheric convective zones over the warmest water to the north of the equator, southerly winds that cross the equator in the Northern Hemisphere, and an eastward oceanic current, the North Equatorial Countercurrent, that has no counterpart south of the equator in the eastern tropical Pacific and Atlantic. Both oceanic and the atmospheric aspects of these asymmetries have been explained as the response of the ocean to the winds and as the response of the atmosphere to sea surface temperature patterns, respectively. Such an approach, however, begs half the answer because the asymmetries should be explained as the response of the coupled ocean–atmosphere–land system to the solar radiation that the earth absorbs. This paper explores how interactions between the ocean and atmosphere contribute to the asymmetries in the equatorial eastern Pacific and Atlantic.

The importance of ocean–atmosphere interactions in the annual cycle of the eastern Pacific and Atlantic Oceans has been demonstrated in recent observational studies (Mitchell and Wallace 1992; Wang 1994). These studies have unambiguously shown that the annual variations of the sea surface temperature (SST) in these regions are highly correlated with fluctuations in the local winds, both zonal component and meridional components. In particular, Mitchell and Wallace (1992) found that the increase in northward wind stress

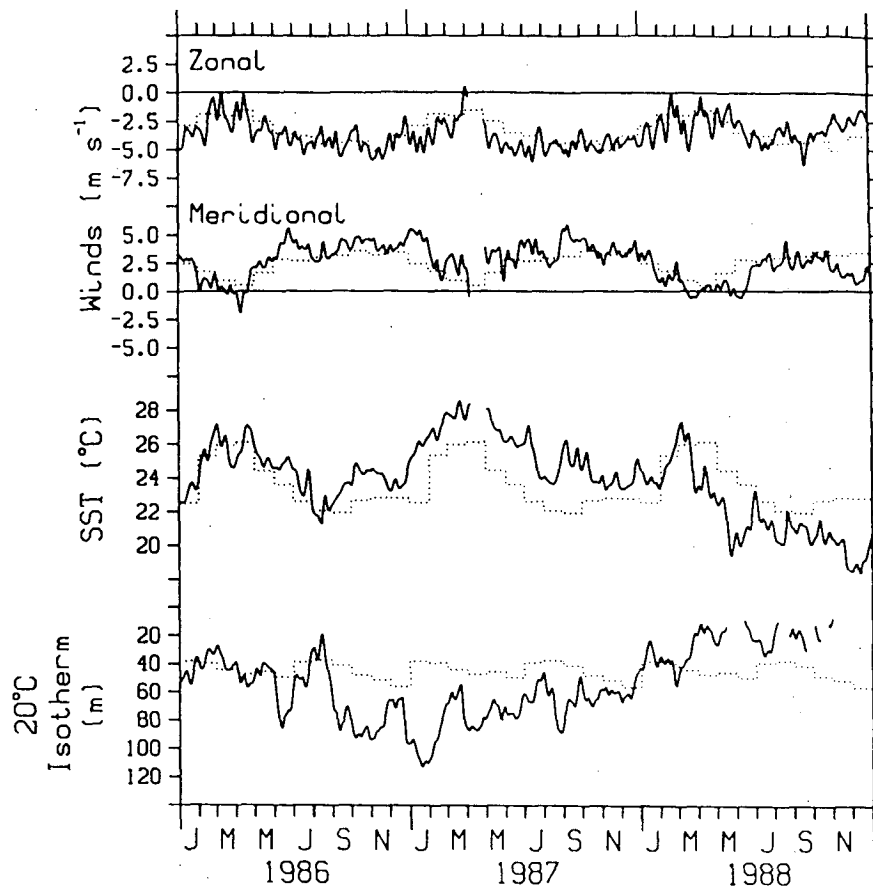*Corresponding author address:* Dr. Ping Chang, Texas A&M University, College Station, TX 77843-3461.

FIG. 1. Time series of zonal and meridional surface wind, SST, and depth of the 20°C isotherm at 0°, 110°W for the three years 1986–88. Solid lines are the measured values, and dotted lines are the monthly mean climatological values based on the historical data from the mooring at this location (from Hayes et al. 1991).

north of the equator occurs simultaneous with, or a month in advance of, the equatorial SST changes. This fact led Mitchell and Wallace to speculate that the meridional wind and its interaction with the local SST gradient may play a crucial role in initiating the annual reappearance of the equatorial cold tongue. At the heart of the Mitchell and Wallace hypothesis lies a positive feedback loop, which can be summarized as follows: in response to the onset of northward wind, cold water upwells to the surface just south of the equator as a result of Ekman divergence. This causes cooling in the atmospheric planetary boundary layer above the cold water, which leads to an increase in the local sea level pressure. The local increase in the sea level pressure enhances the northward pressure gradient immediately to the north of the cold tongue and the westward pressure gradient immediately to the west of the cold tongue, creating positive tendencies in the southerly winds in the north and easterly winds in the west. The intensifying wind stresses promote further upwelling along and south of the equator in the eastern ocean basin. The positive feedback proposed by Mitchell and

Wallace implies an instability in the coupled system that has an antisymmetric SST structure about the equator. However, the nature of such a coupled instability remains to be explored theoretically.

In the eastern tropical Pacific Ocean, the interannual and seasonal sea surface temperature variations are remarkably similar. The cold phase in both cases is characterized by cold waters off the coast of South America and a pronounced equatorial tongue of cold surface waters in the eastern Pacific. The warm phase is marked by the weakening or complete absence of these features. Despite these striking similarities in the SST fluctuations, the subsurface temperature variations are very different on seasonal and interannual timescales. Interannually, a horizontal redistribution of warm surface waters causes the thermocline in the east to deepen during warm periods and to shoal during cold periods. Therefore, the SST variability is highly correlated with the change in thermocline depth. This feature is clearly revealed in Fig. 1, which shows the time series of zonal and meridional surface wind, SST, and depth of the 20°C isotherm from the mooring at 0°, 110°W for the

three years 1986–88. Seasonally, the changes in SST do not seem to be related to the fluctuations in the thermocline depth. The monthly mean climatological values derived from the mooring at 0°, 110°W (Fig. 1) show strong seasonal variations in the sea surface temperature, but minimum fluctuations in the thermocline depth at the equator. From Fig. 2, it is evident that seasonal changes in the depth of the thermocline have a large amplitude to the north of the equator in the eastern Pacific, in a region where seasonal changes in SST are minimal. Interestingly, the seasonal change of SST at the equator appears to be highly correlated with the fluctuations of the local winds (Hayes et al. 1991). This observational evidence suggests that the physical processes that contribute to the ocean–atmosphere interactions on the seasonal timescale are very different from those on the interannual timescale.

Unstable interactions between the ocean and atmosphere have been studied primarily in connection with the Southern Oscillation–El Niño phenomenon. These analyses indicate that it is the shallowness of the thermocline in the eastern tropical Pacific and Atlantic that differentiates those regions from the rest of the tropical oceans. Where the equatorial thermocline is shallow, the dynamical response of the ocean to the winds includes changes in sea surface temperature with an amplitude and spatial scale sufficiently large to affect the atmosphere and hence the winds. This circular argument—winds that affect the ocean which in turn affect the winds—is at the heart of unstable ocean–atmosphere interactions. The analyses performed thus far reveal at least two types of coupled ocean–atmosphere modes: those in which thermocline displacement determines sea surface temperature changes and in which the dominant timescales are associated with the propagation speeds of planetary waves (Hirst 1986; Suarez and Schopf 1988; Battisit and Hirst 1989), and those modes in which the surface Ekman currents and their divergence determine both sea surface temperature changes and the dominant timescales (Neelin 1991). Similar processes undoubtedly play a role in the seasonal cycle, but the available analyses are of limited relevance because they concern ocean–atmosphere modes that are symmetrical about the equator. The seasonal cycle, on the other hand, is primarily antisymmetrical about the equator. This paper focuses on ocean–atmosphere modes that are antisymmetrical about the equator.

The scope of this paper is twofold: first, to explore, by means of both analytical and numerical methods, the existence of the coupled instability modes of relevance to the seasonal cycle in a simple coupled model and, second, to study the properties of these unstable modes and their relation to the symmetric modes. The specific questions to be addressed are the following: Are there any antisymmetric coupled unstable modes in the coupled system? If so, what are the physical processes determining the growth rate and meridional scale of the coupled unstable modes? At what frequency and wavelength does the most unstable wave occur? Finally, What determines the propagation speed and direction of the unstable modes?

The arrangement of the paper is the following: section 2 gives a description of the simple coupled model and the assumptions used to simplify the equations; section 3 discusses the governing eigenvalue problem and the results of the eigenvalue analyses; section 4 describes the numerical results of a simple coupled ocean–atmosphere model, which support the analytical results; and section 5 summarizes the major conclusions.

2. Model and assumption

We explore to what extent ocean–atmosphere interaction can be studied with models complicated enough to include dynamical feedback processes but simple enough to permit analytical analyses. We therefore choose a simple coupled ocean–atmosphere model, which has the Lindzen–Nigam model as the atmospheric component and the Cane–Zebiak model as the oceanic component.

The Lindzen–Nigam model can be written as follows (hereafter we will refer to this model as the LN model):

$$E\tau^x - f\tau^y = -\alpha\left(\frac{\partial\phi}{\partial x} - A\frac{\partial T}{\partial x}\right) \qquad (1)$$

$$E\tau^y + f\tau^x = -\alpha\left(\frac{\partial\phi}{\partial y} - A\frac{\partial T}{\partial y}\right) \qquad (2)$$

$$\phi + B\left(\frac{\partial\tau^x}{\partial x} + \frac{\partial\tau^y}{\partial y}\right) = 0, \qquad (3)$$

where τ^x and τ^y are the zonal and meridional component of the wind stress, ϕ is the geopotential at the top of the boundary layer, T is the sea surface temperature (SST), and E is a mechanical damping due to vertical diffusion of momentum and surface drag. $A = gH_0/2T_0$ and $B = gH_0/\mu\alpha$ measure the strength of the pressure force induced by the SST gradients and the strength of the "back pressure" effect; H_0 is the depth of the boundary layer; T_0 is a reference temperature; μ is an inverse relaxation time for the adjustment of the boundary layer height; and α converts the wind speeds into surface wind stresses. In the LN model, it is assumed the boundary layer temperatures are closely related to SST by turbulent vertical mixing. These horizontal temperature variations induce horizontal pressure gradients, which directly force the low-level atmospheric flow in the Tropics. This flow implies a strong convergence of the boundary layer mass transport, which feeds back to the boundary layer flow through the adjustment of the boundary layer height as the cumulus mass flux responds to boundary layer convergence. To

simulate boundary flow with a reasonable magnitude, the model requires a short adjustment time μ^{-1} of about 30 min and a deep boundary layer of 3000 m. Despite its simplicity, the LN model includes essential dynamical processes of the low-level atmospheric circulation and is capable of capturing the basic seasonal surface wind variability in the eastern tropical Pacific. A more detailed discussion of the LN model can be found in the recent studies by Lindzen and Nigam (1987), Neelin (1989), and Wang and Li (1993).

The oceanic component is an extension of the conventional $1\frac{1}{2}$-layer reduced gravity system that includes the physics of the surface mixed layer and allows prediction of the sea surface temperature. Following Cane (1979), the surface mixed layer model has a constant depth and the entrainment velocity w is determined as the divergence of the surface-layer flow. This simple ocean model has been used widely in the study of El Niño–Southern Oscillation (Cane et al. 1986; Zebiak and Cane 1987; Battisit and Hirst 1989). The recent studies by Seager et al. (1988) and Chang (1994) have demonstrated that the model has considerable skill in simulating the observed seasonal cycle of SST in the tropical Pacific Ocean when forced with realistic heat flux. (Hereafter this model will be refered to as the CZ model.)

The CZ model has recently been studied in a great detail by Neelin (1991) to identify the symmetric coupled unstable modes that are relevant to ENSO. He shows that if the coupling timescales determined by the interaction between SST and winds are much longer than the timescale of wave propagation across the basin, then the coupled modes fall into two classes: the slow SST mode and the relatively fast modified oceanic mode. For the SST mode, the interaction between the ocean and atmosphere basically occurs within the surface boundary layer, and the ocean dynamics influences the SST variability mainly through the change in the thermocline depth, which is in balance with the local wind stresses. It means that one can neglect the horizontal advection of heat due to the geostrophic currents u and v, and the SST equation in the CZ model can be simplified as follows:

$$T_t + \bar{u}_1 T_x + \bar{v}_1 T_y + \frac{\bar{w}}{H_1}(T - \gamma h) + u_1 \bar{T}_x$$

$$+ v_1 \bar{T}_y + w \bar{T}_z + \epsilon T - \kappa \nabla^2 T = 0 \quad (4)$$

$$\begin{bmatrix} u_1 \\ v_1 \end{bmatrix} = \frac{H_2}{H} \begin{bmatrix} u_e \\ v_e \end{bmatrix}, \quad w = \frac{H_1 H_2}{H} \nabla \cdot \mathbf{v}_e \quad (5)$$

$$\begin{bmatrix} u_e \\ v_e \end{bmatrix} = \frac{1}{\Delta_0} \begin{bmatrix} r_s \tau^x + f \tau^y \\ r_s \tau^y - f \tau^x \end{bmatrix}, \quad \Delta_0 = H_1(r_s^2 + f^2), \quad (6)$$

where H_1 and H are the depth of the mixed layer and the mean depth of the thermocline; H_2 is defined as the difference between H and H_1; $\bar{u}_1$, $\bar{v}_1$ and u_1, v_1 represent the zonal and meridional component of the mean and

anomalous surface currents; $\bar{w}$ and w denote the mean vertical upwelling and the anomalous upwelling due to the surface Ekman divergence; γ is a parameter that relates the entrained subsurface water to the thermocline depth; r_s is the linear damping coefficient in the mixed layer; and ϵ and κ are the linear damping and diffusion coefficient in the temperature equation.

Interannual sea surface temperature changes in the eastern tropical Pacific—those associated with El Niño—are caused primarily by a horizontal redistribution of warm surface waters. This redistribution causes the thermocline in the east to deepen during warm periods and shoal during cold periods. Very different physical processes control seasonal sea surface temperature changes. Figure 2, which shows the standard deviation of temperature at different depths in the tropical Pacific Ocean, reveals that the subsurface temperature fluctuations below 50 m over the equatorial Pacific cold tongue are considerably weaker than that near the surface. Observational studies (Hayes et al. 1991; Chang 1993) confirm that the seasonal temperature variations are confined to the surface mixed layer. The recent ocean general circulation model study by Koeberle and Philander (1994) and Chang's (1994) study with a very different model demonstrate that in the Pacific cold tongue region the surface heat flux plays an important part in the seasonal cycle of SST, more so than the vertical movements of the thermocline. These results imply that the strong annual cycle of the eastern equatorial Pacific is in part attributable to the interaction between the two boundary layers in the coupled ocean–atmosphere system and that the subsurface oceanic dynamics plays a minor role in the seasonal variation of the SST in this region. On the basis of this observational and modeling evidence, it is argued that 1) the coupled SST modes are most relevant to the annual development of the cold tongue/ITCZ complex and 2) the change in the thermocline depth has little effect on the SST modes of relevance to the seasonal cycle, so that γ in (4) can be set to zero and the SST change is completely decoupled from the ocean dynamic processes. These assumptions will be further verified by the numerical experiments of a coupled ocean–atmosphere model in section 4.

3. Linear instability analysis

If the solutions are of the form $T(y) \exp(\sigma t + ikx)$, then Eqs. (1)–(4) form an eigenvalue problem with σ being the eigenvalue and k being the zonal wavenumber. The problem can be solved numerically using matrix methods to obtain dispersion relations for the coupled unstable modes. However, before proceeding to the numerical solution, some basic properties of the governing eigenvalue problem can be obtained by examining the solution at the long-wave limit $k = 0$.

a. The coupled unstable modes at the long-wave limit

In the long-wave limit, $k = 0$; if it is of the form $\tau^y = \tau(y)e^{\sigma t}$, Eqs. (1)–(4) can be reduced, by assuming $\gamma = \bar{T}_x = 0$, to a single eigenequation for the meridional wind stress τ:

$$\kappa \frac{d^2}{dy^2}D(\tau) - \frac{d}{dy}[\bar{v}_1 D(\tau)]$$

$$- \left(\frac{\bar{W}}{H_1} + \epsilon\right)D(\tau) - \frac{H_2}{EHH_1}\frac{d}{dy}\left[\bar{T}_y \frac{\Delta}{\Delta_0}\tau\right]$$

$$- \frac{H_2}{EH}\frac{d^2}{dy^2}\left[\bar{T}_z \frac{\Delta}{\Delta_0}\tau\right] = \sigma D(\tau), \quad (7)$$

where

$$D(\tau) = -\frac{B}{A}\frac{d^2\tau}{dy^2} + \frac{\Delta_a\tau}{H_1 E\alpha A},$$

$$\Delta = H_1(r_sE - f^2), \quad \Delta_a = H_1(E^2 + f^2).$$

The boundary conditions for the governing eigenvalue problem are

$$\tau = \frac{d\tau}{dy} = 0 \quad \text{as} \quad y \to \pm\infty. \quad (8)$$

Equation (7) is a fourth-order differential equation whose coefficient for the highest-order derivative is the diffusion coefficient κ. In the absence of diffusion, mean currents, and mean temperature gradients; that is, $\kappa = \bar{v}_1 = \bar{w} = \bar{T}_y = \epsilon = 0$, Eq. (7) reduces to a second-order differential equation that can be converted into a compact form by a simple transformation $Q = P(\eta, \sigma)\tau$:

$$\frac{d^2Q}{d\eta^2} + \frac{R(\eta, \sigma)}{P(\eta, \sigma)}Q = 0, \quad (9)$$

where

$$R(\eta, \sigma) = \frac{\sigma r_s}{\alpha A}\left(\frac{1}{r} + \eta^2\right),$$

$$P(\eta, \sigma) = \frac{H_2\bar{T}_z}{HEL^2}\frac{1 - \eta^2}{r + \eta^2} - \frac{B\sigma}{AL^2}, \quad (10)$$

$r = r_s/E$ is the ratio of the linear friction in the oceanic mixed layer to the linear friction in the atmospheric boundary layer, $L = \sqrt{Er_s}/\beta$ defines a frictional characteristic length scale that determines the distance away from the equator beyond which the Coriolis effect dominates over the frictional effect in the boundary layer, and η is the nondimensionalized latitude y; that is, $\eta = y/L$. The corresponding boundary conditions for (9) are $Q = 0$ as $\eta \to \infty$.

The quantity $l^2 = R(\eta, \sigma)/P(\eta, \sigma)$ defines the refraction index. The trapped wave solutions can only exist in the region where l^2 is positive. Figure 3 shows
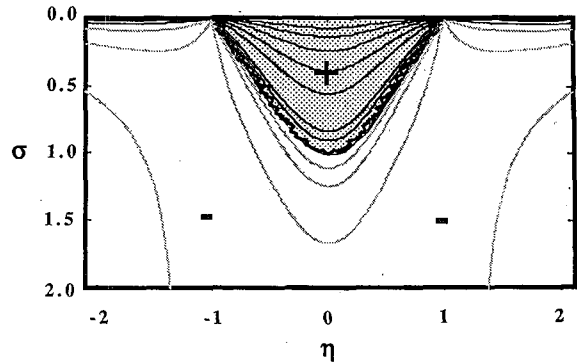
$R(\eta, \sigma)/P(\eta, \sigma)$ as function of η and σ

FIG. 3. Distribution of the refraction index $l^2 = R(\eta, \sigma)/P(\eta, \sigma)$ as a function of η and σ. The shaded area is the region where the coupled instability could occur. This region is bounded by a curve $P(\eta, \sigma) = 0$.

the refraction index as a function of η and σ. The region where both l^2 and σ are positive is shaded, and its boundary is determined by $P(\eta, \sigma) = 0$. The latitudinal extent of this region, in which the interaction between the ocean and atmosphere produce coupled instability, depends on the frictional length L. Physically, this can be understood by invoking the following positive feedback mechanism: near the equator where $|y| < L$, the linear friction dominates the Coriolis effect in both the atmospheric and oceanic boundary layers. Therefore, the Ekman drift in the ocean flows in the direction of the surface winds, and the winds are in the direction of the SST gradients. Under such conditions, an anomalous southerly wind near the equator generates Ekman divergence to the south of the equator by intensifying the cross-equatorial Ekman drift and causes cooling of the surface water. The cooling in the south enhances the northward temperature gradient near the equator, which in turn amplifies the southerly wind anomaly. This positive feedback mechanism is responsible for the coupled instability. However, in the off-equatorial regions where $|y| > L$ such a mechanism will not work. This is because the Coriolis effect dominates the frictional effect in these regions, and the Ekman drift is in a direction perpendicular to the surface wind stresses. Consequently, it cannot produce Ekman upwelling and the surface cooling required for the positive feedback mechanism is absent.

The governing eigenvalue problem (9) has singularities at $P(\eta, \sigma) = 0$. They are similar to the critical layer that waves encounter when propagating in the shear flow, although the asymptotic solutions as friction goes to zero are different. Because of those singularities, the governing eigenvalue problem has a continuum of "unsmooth" eigenmodes given by

$$P(\eta, \sigma) = 0, \quad \text{or} \quad \sigma = \frac{AH_2\bar{T}_z}{HEB}\frac{1 - \eta^2}{r + \eta^2}. \quad (11)$$

Obviously, the maximum growth rate occurs at $\eta = 0$ (or $y = 0$) where

$$\max(\sigma) = \frac{\mu\alpha H_2 \bar{T}_z}{2T_0 H r_s}. \tag{12}$$

From Eq. (12), it is clear that the maximum growth rate increases as the mean vertical temperature gradient $\bar{T}_z$ increases, but decreases as the adjustment time of the atmospheric boundary layer height μ^{-1} and the linear friction r_s in the oceanic mixed layer increase. For a typical condition in the eastern Pacific where $E = 1/2.5$ day^{-1}, $r_s = 1/2$ day^{-1}, $\mu = 1/30$ min^{-1}, $\alpha = 1.27 \times 10^{-5}$ m s^{-1}, $H_1 = 20$ m, $H = 50$ m, $\bar{T}_z = 0.20°$C km^{-1}, the characteristic length scale of the unstable modes L is about 225 km and the maximum growth rate is approximately $1/47$ day^{-1}. In the western Pacific where $\bar{T}_z$ is much smaller (about $0.05°$ km^{-1}), the maximum growth rate σ_{max} decreases to $1/365$ day^{-1}. Note that in deriving (12) we assumed that the value of the Newtonian cooling coefficient ϵ is zero. In reality, a value of order $1/150$ day^{-1} may be reasonable due to surface heat flux damping of SST anomalies in a mixed layer 50 m deep. Therefore, the actual maximum growth rate should be equal to the quantity given by (12) minus the damping rate ϵ, which gives a smaller value of $\max(\sigma)$ on the order of $1/70$ day^{-1}. It is understood that the growth rate $\mathrm{Re}(\sigma)$ presented below is referenced to the damping rate ϵ.

Finding structures of the "unsmooth" eigenmodes can be cumbersome analytically. It usually requires the use of Frobenius method near the singularity. However, the precise form of the singular mode need not concern us here, because diffusion $\kappa\nabla^2 T$ in the SST equation will remove the singularities in the eigenvalue problem (9). When diffusion is retained, the governing eigenvalue problem given by Eq. (7) has a discrete set of unstable modes whose eigenvalues lie between 0 and σ_{max}. Figure 4 shows the meridional structures of τ for different values of κ. It is clear from Fig. 4 that the most unstable mode has a symmetric meridional wind structure about the equator and an antisymmetric SST structure. Both the eigenvalues and the structure of the eigenvectors are dependent upon the diffusivity κ. As κ increases, the meridional length scale of the eigenmode increases, but the growth rate decreases. When diffusivity κ is beyond a certain value (approximately 10^4 m^2 s^{-1} for the given parameters), no instability can occur. It is interesting to note that all the eigenvalues appear to be real, indicating that the unstable modes are nonoscillatory and have zero frequency at the long-wave limit.

b. Dispersion relation for the unstable modes

The general eigenvalue problem $(1)-(4)$ can be solved numerically to obtain dispersion relations for the coupled modes. The results presented below are obtained by a finite-difference method that discretizes the differential equations $(1)-(4)$ into a matrix equation. The solution procedure is similar to the one described by Hirst (1986). The computational domain spans from $L = -5$ to $L = 5$. The spatial resolution is 0.05. The parameters used in the computation are listed in Table 1.

First, we examine the properties of coupled instability in the absence of mean background fields, that is, $\bar{u}_1 = \bar{v}_1 = \bar{w} = \bar{T}_y = 0$. Figure 5 shows the dispersion diagrams of both antisymmetric and symmetric unstable SST modes for a diffusivity $\kappa = 100$ m s^{-2}. It is clear from these diagrams that the growth rate of the antisymmetric SST mode has maximum value (about $1/40$ day^{-1}) at $k = 0$ and decreases monotonically as k increases. The frequency, on the other hand, increases initially from zero as k increases until reaching maximum value of approximately $2\pi/5340$ day^{-1} at $k \approx 2\pi/3534$ km^{-1} and then decreases monotonically as k increases further. For small k, the frequency associated with the antisymmetric SST mode is positive, indicating that the long antisymmetric SST mode has a tendency to propagate eastward. The unstable symmetric SST mode has smaller growth rate than the antisymmetric mode. The maximum growth rate is about $1/48$ day^{-1} and again occurs at $k = 0$. In contrast to the antisymmetric mode, the frequency of the symmetric SST mode is negative at all wavelengths, indicating a westward phase propagation. In the long-wave limit, the waves are nearly nondispersive. The maximum phase speed for the most unstable symmetric mode is about 1.3 cm s^{-1}. Figures 6a and 6b depict the structures of the SST and wind stresses for the most unstable antisymmetric and symmetric SST modes, respectively, at $k = 0$. As expected, for the antisymmetric mode, a southerly (northerly) wind anomaly near the equator corresponds to a cold (warm) SST anomaly to the south of the equator and a warm (cold) SST anomaly to the north. For the symmetric SST mode, a divergence (convergence) of meridional wind anomalies is responsible for a cold (warm) SST anomaly at the equator. This symmetric mode is essentially the Neelin's SST mode (Neelin 1991). As predicted by the theory, the meridional extents of both the antisymmetric and symmetric SST modes are confined by the frictional scale L.

Next, we examine the effects of zonal-mean current and zonal-mean temperature gradient on the coupled unstable modes. For simplicity, the zonal-mean current is assumed to be an isolated westward Gaussian jet centered at the equator, and the zonal-mean temperature gradient is set to be a constant value of 5×10^{-4} °C km^{-1}. The jet has an e-folding width of deformation radius $\sqrt{C/\beta}$ (355 km) and a maximum westward velocity of 30 cm s^{-1}. Figures 7a and 7b show the growth rates and frequencies of the most unstable antisymmetric and symmetric SST modes. It is evident from Fig. 7a that the mean background fields have mi-
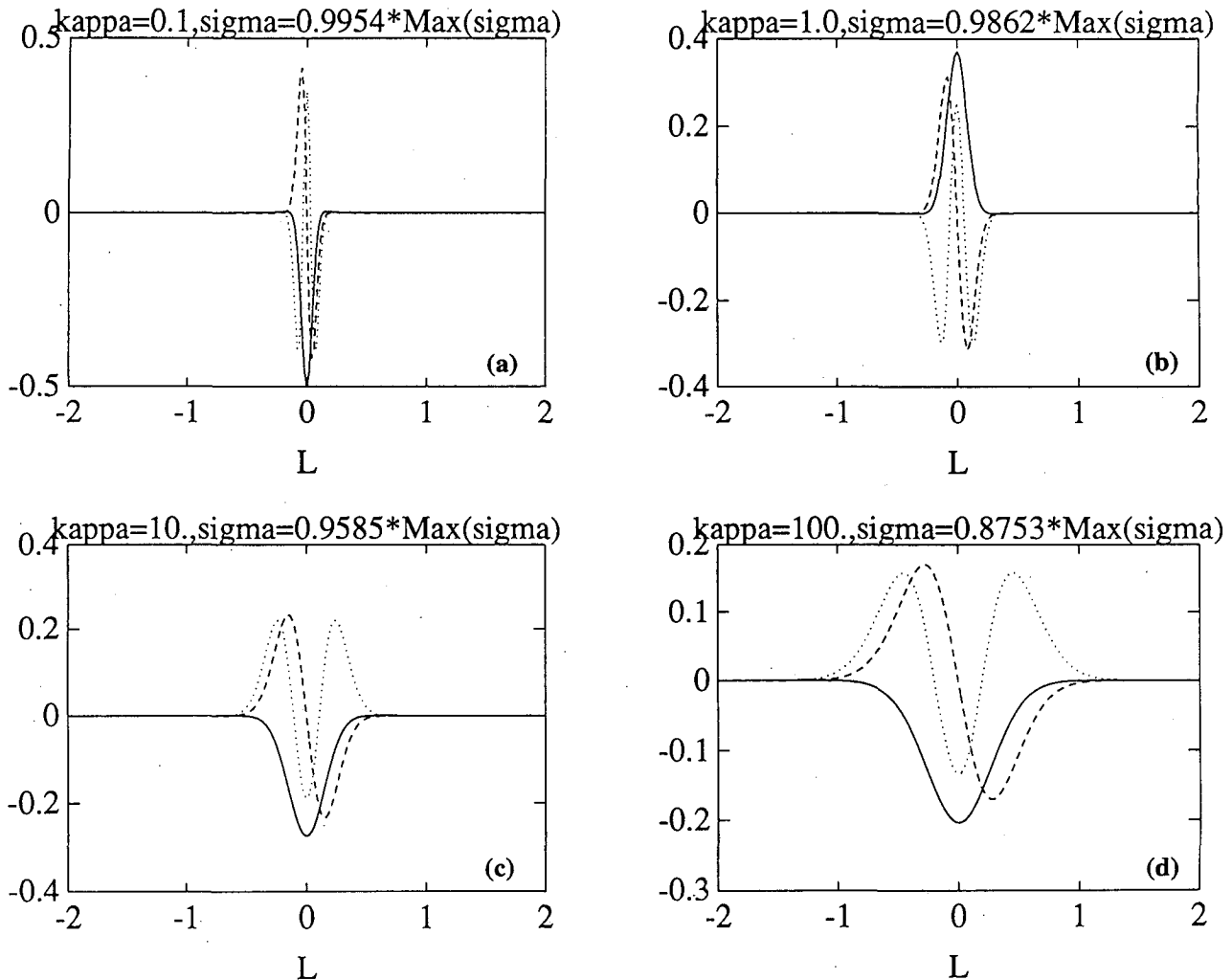
FIG. 4. Meridional structure τ^y of the first three most unstable modes for (a) $\kappa = 0.1$ m^2 s^{-1}, (b) $\kappa = 1.0$ m^2 s^{-1}, (c) $\kappa = 10.0$ m^2 s^{-1}, and (d) $\kappa = 100.0$ m^2 s^{-1}. The corresponding maximum growth rates are $0.9954\sigma_0$ in (a), $0.9862\sigma_0$ in (b), $0.9585\sigma_0$ in (c), and $0.8753\sigma_0$ in (d), where σ_0 is the maximum growth rate in the absence of diffusion.

nor effects on the growth rates of the unstable modes, especially at long-wave limit. The maximum growth rates still occur at zero wavenumber, and their values remain almost unchanged from the previous case. However, the frequencies and propagation speeds of the modes are dramatically modified by the presence of the mean current. As shown in Fig. 7b, the propagation speeds of both the antisymmetric and symmetric modes are essentially determined by the mean current speed along the equator. This result is consistent with the analytical solutions obtained by Neelin (1991), who showed that the zonal advection of heat by mean currents contribute mainly to propagation rather than growth characteristics of the SST mode. To examine the relevance of the SST modes to the observed annual cycle of SST and surface winds in the eastern Pacific and Atlantic, Figs. 8a and 8b exhibit structures of the

antisymmetric and symmetric modes at the annual period (the corresponding wavelength is about 9500 km). Of particular interest is the structure of the annual symmetric mode (Fig. 8b), in which the anomalous westerly (easterly) winds appear to the west of anomalous warm (cold) sea surface temperature anomalies. This feature bears a resemblance to the observed seasonal SST and zonal wind anomalies along the equator (Wang 1994), suggesting that the westward propagating feature in the annual cycle of near-equatorial zonal wind and SST in the eastern Pacific and Atlantic Oceans may correspond to the annual symmetric SST mode.

Finally, we examine the dependence of the maximum instability growth rate on the model parameters. The analytical result given by Eq. (12) indicates that the growth rate is linearly proportional to the mean ver-

TABLE 1. Parameters used in linear instability analysis.

Symbol	Parameter	Value
E	Mechanical damping coefficient in atmospheric boundary layer	$1/2.5$ day^{-1}
H_0	Depth of atmospheric boundary layer	3000 m
μ	Newtonian damping coefficient in atmospheric boundary layer	$1/30$ min^{-1}
α	Coefficient converting wind speeds to wind stresses	1.586×10^{-5} m s^{-1}
T_0	Reference temperature	300.15 K
H_1	Depth of oceanic mixed layer	50 m
H	Depth of thermocline	150 m
r_s	Mechanical damping coefficient in oceanic mixed layer	$1/2$ day^{-1}
$\bar{T}_z$	Mean vertical temperature gradient	0.2 K m^{-1}
κ	Diffusion coefficient	100 m^2 s^{-1}

tical temperature gradient $\bar{T}_z$ and coefficient α, but inversely proportional to frictional coefficient r_s. To verify this result, we compute the growth rates and frequencies of the most unstable antisymmetric and symmetric SST (at $k = 0$) as functions of model parameters $\bar{T}_z$, r_s, and α. While varying the selected model parameters ($\bar{T}_z$, r_s, and α), the other model parameters and the mean background fields are kept the same as those in the previous calculation. The results are illustrated in Figs. 9a and 9b, which clearly demonstrate that for both the antisymmetric SST mode (Fig. 9a) and symmetric SST mode (Fig. 9b) the growth rates increase almost linearly as $\bar{T}_z$, r_s^{-1}, and α increase. This result is consistent with the analytical solution (12).

4. Numerical experiment of a coupled model

To support the results of the eigenvalue analyses, we conduct a number of numerical experiments using an intermediate coupled atmosphere–ocean model. The atmospheric component of the model is a "new" 2-level model of the free atmosphere above an atmospheric boundary layer developed by Wang and Li (1993). This model incorporates Gill's atmospheric model with Lindzen and Nigam's boundary layer model and allows active interactions between the boundary layer flow driven by SST gradient and the free-tropospheric flow driven by diabatic heating stimulated by the thermal forcing of SST. The extensive model simulations and the model sensitivity studies by Wang and Li (1993) have demonstrated that the new model is more realistic than the previous simple atmospheric models and is capable of simulating the seasonality of the surface winds in the tropical Pacific when forced with realistic SSTs as the model boundary condition. In particular, the model is successful in reproducing both the intertropical convergence zone (ITCZ) and the South Pacific convergence zone

(SPCZ). A brief description of the model formulation and a summary of the model parameters are given in the appendix. A more detailed discussion can be found in Wang and Li (1993).

The oceanic component is essentially the same model used by Seager et al. (1988) with a simpler parameterization scheme for the subsurface temperature change given by

$$T_d = \bar{T}_{sub} + \partial_z\bar{T}_{sub}(h - \bar{h}), \qquad (13)$$

where $\bar{T}_{sub}$ and $\partial_z\bar{T}_{sub}$ are the subsurface mean temperature and its vertical derivative. Seager et al. (1988) and Chang (1994) have shown that the model is capable of capturing the essential seasonal SST variability in the tropical Pacific when forced with the climatological surface winds and heat flux forcing. In particular, these studies have demonstrated that the simple ocean model has considerable skill in simulating the observed seasonal cycle of SST in the tropical eastern
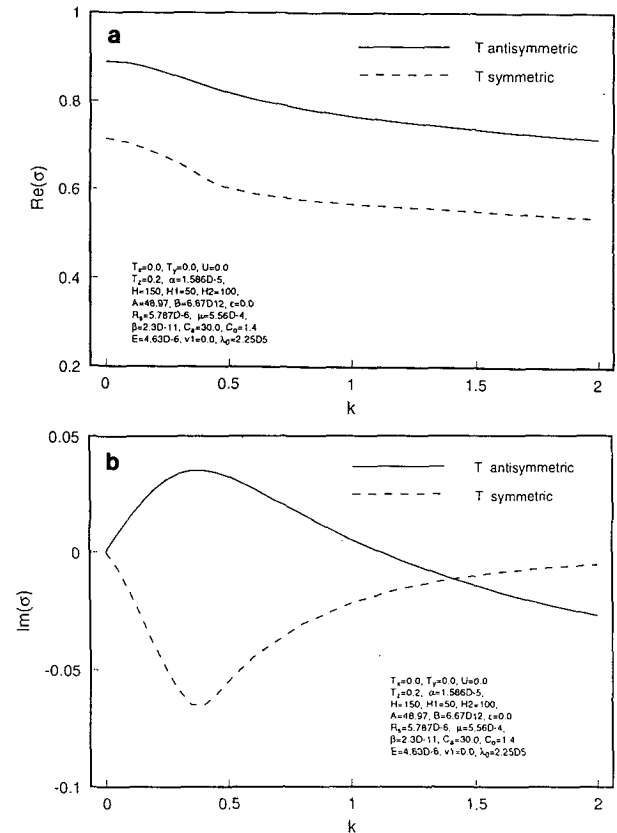

FIG. 5. Dispersion diagram of the most unstable coupled antisymmetric and symmetric SST modes in the absence of mean background fields: (a) the growth rate Re(σ) of the antisymmetric SST mode (solid line) and the symmetric SST mode (dashed line); (b) the frequency Im(σ) of the antisymmetric SST mode (solid line) and the symmetric SST mode (dashed line). In the figures Re(σ) and Im(σ) are nondimensionalized by max(σ) $= \mu\alpha H_2\bar{T}_z/(2T_0Hr_s)$, and k is nondimensionalized by $L^{-1} = \beta/\sqrt{Er_s}$.
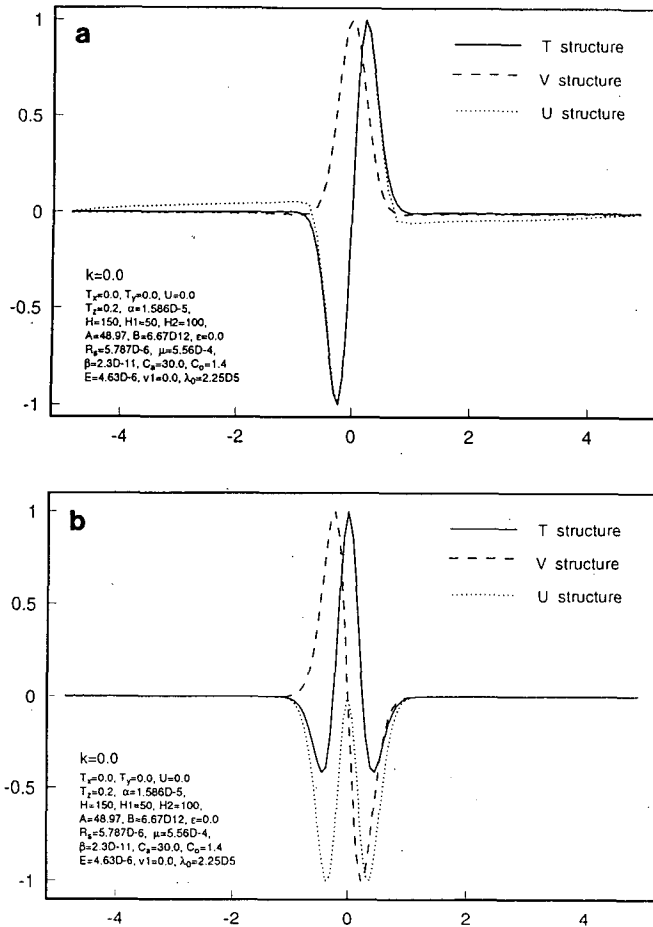
FIG. 6. Structure of (a) the antisymmetric SST mode and (b) the symmetric SST mode at $k = 0$. In the figures, SST is plotted by solid line, and the zonal and meridional components of wind are plotted by dotted and dashed lines, respectively. The x axis is measured by the frictional scale $L = \sqrt{Er_s/\beta}$.

Pacific Ocean. A summary of the model equations and model parameters can be found in the appendix.

The atmospheric and oceanic components are coupled using a simple linear relation between surface wind stresses and wind speeds; that is, $(\tau_x, \tau_y) = \alpha(U, V)$, where α is a coupling coefficient of value $\alpha = 1.27 \times 10^{-5}$ m s^{-1}. The coupling is done every 2 model days. The numerical scheme used to solve the model equations is a second-order finite-difference scheme with leapfrog time stepping and a weak Robert smoothing with a coefficient of 0.005. The temperature equation (3) is solved using the density-conserving form of the finite-difference scheme to retain numerical accuracy. The model resolution is 1 degree in longitude and 0.5 degrees in latitude. The model domain extends from 30°S to 30°N in latitude and 160° in longitude. No-flux boundary conditions in temperature and free-slip boundary conditions in velocity are applied at the boundaries of model ocean.

Two sets of numerical experiments are performed. In the first set of experiments, the model ocean contains no mean currents, and the mean temperature in the mixed layer is set uniformly at 27°C. The subsurface temperature $\bar{T}_{sub}$ and its derivative $\partial_z\bar{T}_{sub}$ are chosen to be 18°C and 0.1°C m^{-1}. At time $t = 0$, a weak, zonally uniform, antisymmetric temperature anomaly given by

$$T(x, y, 0) = 27°C + 0.5°C \tanh(y/L_y) \quad (14)$$

is introduced to the coupled system, where L_y is set to be 1000 km. The model is then integrated in time with no external forcing to examine the time evolution of the initial temperature anomaly. Figures 10a and 10b show the latitude–time plots of the mixed layer temperature and the meridional wind stress taken at the center of the basin from a control run where $r_s^{-1} = 1$ day and $H_1 = 50$ m. The vectors in the figures indicate the strength of the Ekman upwelling/downwelling and the meridional Ekman drift. (A vector that points up
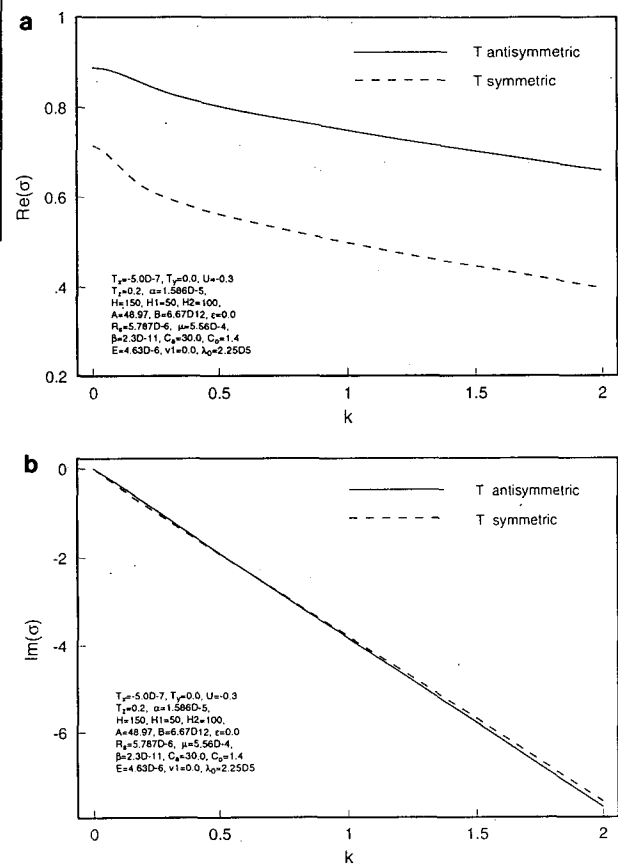

FIG. 7. Dispersion diagram of the most unstable antisymmetric and symmetric SST modes in the presence of mean background fields: (a) the growth rate Re(σ) of the antisymmetric SST mode (solid line) and the symmetric SST mode (dashed line) and (b) the frequency Im(σ) of the antisymmetric SST mode (solid line) and the symmetric SST mode (dashed line); σ and k are nondimensionalized as in Fig. 4.

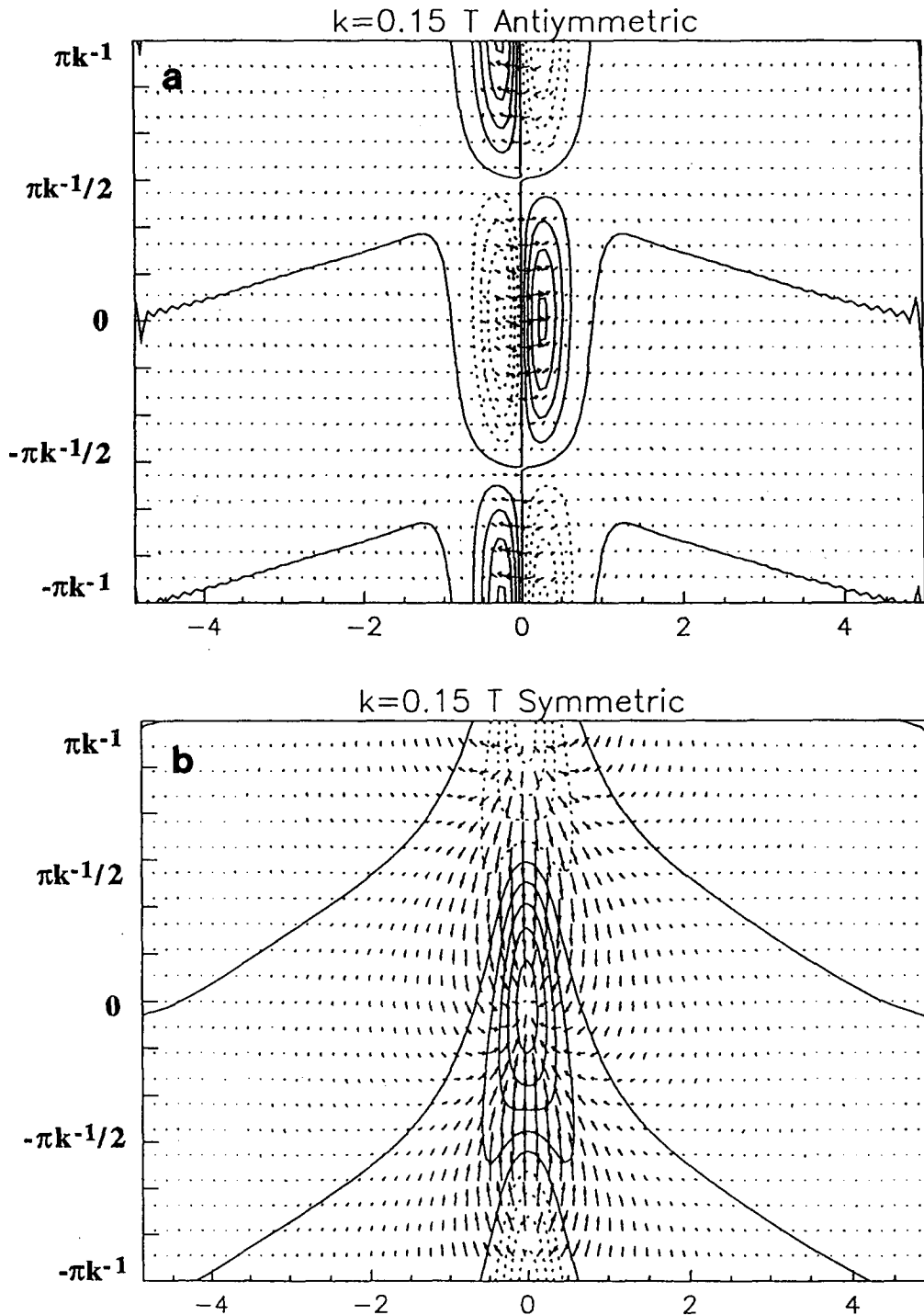## k=0.15 T Antiymmetric

k=0.15 T Symmetric

FIG. 8. Structure of SST (contour) and wind stresses (vector) for (a) the most unstable antisymmetric SST mode and (b) the most unstable symmetric SST mode at $k = 0.15$ (the corresponding wavelength and period are about 9500 km and one year, respectively). The x axis is measured by the frictional scale $L = \sqrt{Er_s/\beta}$.

indicates upwelling; one that points to the right indicates northward flow.) The time evolution of the anomalous temperature and wind fields can be roughly divided into two stages. During the first stage (between

$t = 30$ and 60 days), the linear instability dominates and the mixed layer temperature undergoes a rapid cooling to the south of the equator (maximum cooling occurs approximately at 2°S). As shown in Fig. 10b,
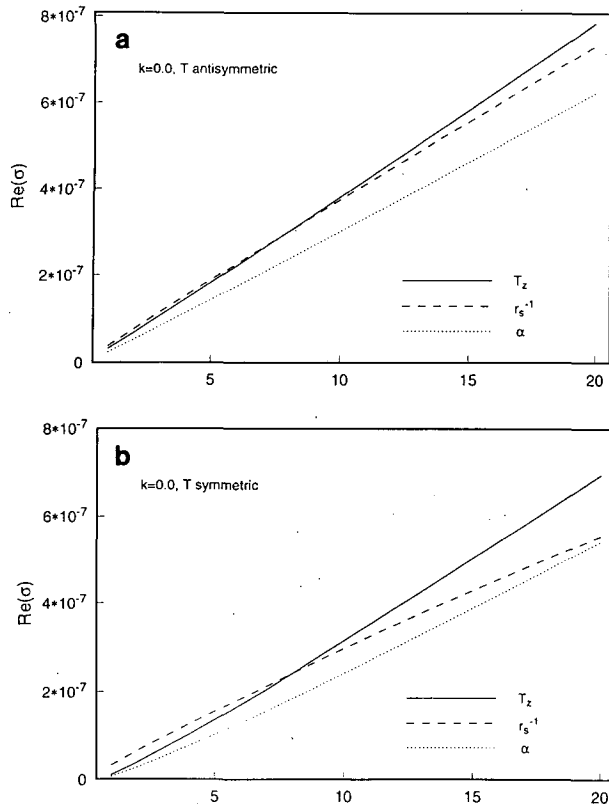
FIG. 9. The change of growth rate Re(σ) for (a) the antisymmetric and (b) symmetric SST mode at $k = 0$ as a function of parameters r_s^{-1} (solid), $\bar{T}_z$ (dashed), and α (dot–dashed). In the figure, the changes of $\bar{T}_z$, α, and r_s^{-1} are expressed in terms of a single parameter P, that is, $\bar{T}_z = \bar{T}_{z0}P$, $\alpha = \alpha_0 P$, and $r_s^{-1} = r_{so}^{-1}P$, where $\bar{T}_{z0} = 0.025°C\ m^{-1}$, $\alpha_0 = 1.586 \times 10^{-6}\ m\ s^{-1}$, $r_{so}^{-1} = 0.25$ day, and P varies from 1 to 20.

the strong surface cooling is apparently caused by the strong Ekman upwelling induced by the divergence of the meridional wind stress in the region. This result supports the findings of the eigenvalue analyses that the positive feedback between the meridional wind and SST gradient is responsible for the coupled instability. However, unlike the antisymmetric temperature structure indicated by the eigenvalue analyses, the temperature anomaly shown in Fig. 10a is asymmetric about the equator. The asymmetry is manifested in the north of the equator where no surface warming is observed, even though strong Ekman downwelling is present. This is because the nonlinearity associated with vertical advection of heat in the model permits cooling due to the upwelling but inhibits warming due to the downwelling. The other feature absent in the linear antisymmetric SST mode is the southward wind south of the equator. This wind anomaly is apparently produced by the strong SST gradient south of the equator. Its presence is partially due to the equatorial asymmetry of the SST in the model, which gives relatively weak northward SST gradient at the equator, and thus relatively

weak northward cross-equatorial wind in comparison with the linear antisymmetric SST mode. The linear growth rate of the instability can be estimated by first computing the logarithmic changes of the temperature minimum at given longitude as a function of time and then performing a linear regression. The resultant growth rate for the chosen parameters is about $1/14$ day^{-1}.

During the second stage, the nonlinear advection appears to be dominant. After the onset of the coupled instability, the cold surface temperature anomaly to the south of the equator is advected rapidly poleward by the meridional surface currents induced by the strong meridional wind stress. As the temperature fronts are advected away from the equator, the meridional temperature gradient in the wake of the fronts quickly decreases, which causes a weakening of the positive feedback loop and reduces the growth of the temperature anomaly. To further examine the role of meridional heat advection, a run without the horizontal advection of heat was made. Figures 10c and 10d show the time evolution of the SST and meridional wind in such a case. Clearly, in comparison with the control run the anomaly fields exhibit much less extensive poleward expansion. The meridional scale of the coupled mode in this case is essentially determined by the linear theory $L = \sqrt{Er_s/\beta}$, which has a value of 468 km for the given model parameters.

Additionally, we have performed sensitivity experiments with different shapes of initial disturbances to test whether the response of the model is sensitive to the choice of initial conditions. The results show that the growth of antisymmetric mode in the model is independent of the detailed structure of the initial conditions provided that the initial disturbance contains a small meridional SST gradient near the equator. It suggests that the antisymmetric mode is indeed the most unstable mode in the system. Moreover, in the absence of a mean background state, a cold tongue can appear on either side of the equator depending upon the sign of the meridional SST gradient in the initial SST.

The eigenvalue analysis indicates that the coupled instability depends on certain model parameters. To examine the sensitivity of the coupled instability to a change in model parameters, three sets of numerical experiments are performed. In each set of experiments, a single model parameter is chosen to be adjustable while other parameters are kept the same as in the control case. In all the experiments, the same initial condition given by (14) is used. First, we chose the linear frictional coefficient in the oceanic mixed-layer r_s to be the varying parameter. Five different values are assigned to r_s, that is, $r_s = 1/0.25, 1/0.5, 1/2$, and $1/3$ day^{-1}. The estimated growth rate, as shown in Fig. 11, increases almost linearly as r_s^{-1} increases. This result is consistent with the analytical solution given by Eq. (12), which indicates that the maximum growth rate of
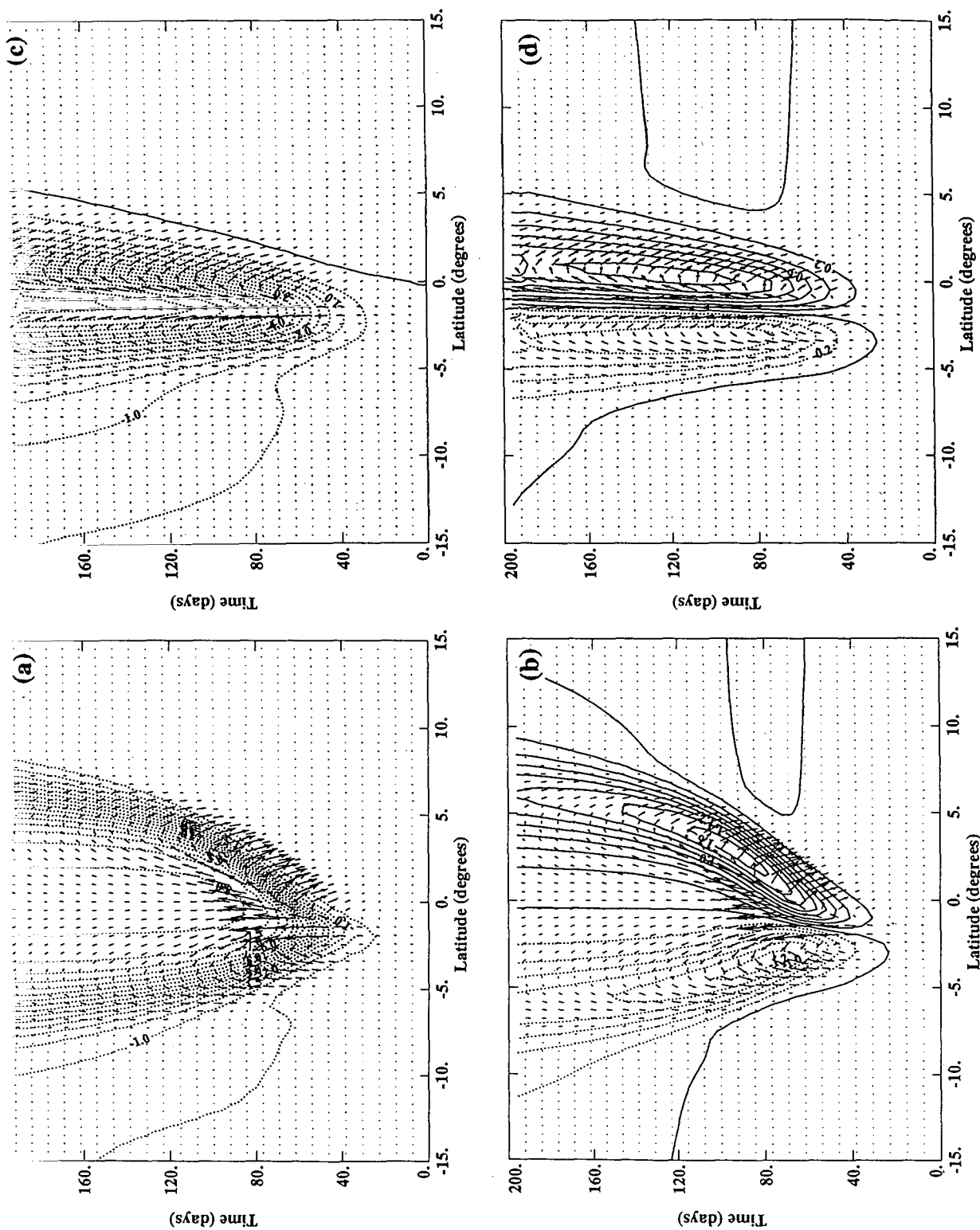
FIG. 10. Time–latitude plots of (a) the SST and (b) the meridional wind stress taken at the center of the basin from the control run. (c) and (d) show the similar plots of the SST and meridional wind stress for the run where the advection of heat is removed from the SST equation. To illustrate effects of the Ekman upwelling/downwelling and the meridional Ekman drift, vectors are plotted in the figures by rescaling the vertical component of the velocity to a comparable magnitude of the meridional velocity. Contour intervals are 0.5°C in (a) and (c) and 0.2 dyn cm⁻² in (b) and (d).
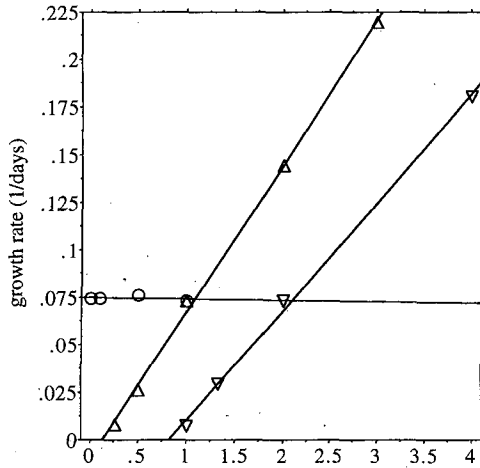
FIG. 11. Estimated growth rates in the coupled model as a function of model parameters: $\triangle$ indicates the values of r_s^{-1} (days), O indicates the values of $\partial_z \bar{T}_{sub}$ (°C m^{-1}), and ∇ indicates the values of H_1^{-1} $\times 10^2$ (m). Fitted data using linear regression is shown by solid lines.

the antisymmetric SST mode is linearly proportional to r_s^{-1}. In the second set of experiments, $\partial_z \bar{T}_{sub}$ is taken to be 0., 0.1, 0.5, and 1.0°C m^{-1}, respectively, in four different runs. The result shown in Fig. 11 indicates that the growth rate of the coupled instability is insensitive to the changes in $\partial_z \bar{T}_{sub}$. Since $\partial_z \bar{T}_{sub}$ is a measure of the effect of the thermocline depth change on the entrained subsurface temperature, it implies that varying thermocline depth has little influence on the coupled instability. This is again in agreement with the analytical result given by (12), which shows that the growth rate of the instability is independent of the changes in the thermocline depth. Finally, in the third set of experiments, the depth of the model mixed layer h_1 is varied and its value is set to be 100, 75, 50, and 25 m. Figure 11 shows that the growth rate increases linearly as H_1^{-1} increases. This can be shown to be consistent with Eq. (12). In the coupled model the mean temperature vertical gradient is approximately given by $\bar{T}_z = \Delta \bar{T}/H_1$. Using this approximation in Eq. (12), it is readily shown that the maximum growth rate of the antisymmetric mode is proportional to $\Delta \bar{T}(H_1^{-1} - H^{-1})$. Since $\Delta \bar{T}$ is a constant in the model, one anticipates that the growth rate increases linearly as H_1^{-1} increases. Therefore, all the numerical results presented here are complementary to the eigenvalue analyses.

In the aforementioned experiments, the mean condition of the coupled system has been assumed to be uniform. In reality, however, the observed annual-mean conditions in the eastern Pacific and Atlantic exhibit the marked equatorial asymmetries. To examine the effects of the realistic mean state on the coupled instability, an additional experiment is performed with a mean state that resembles the observed annual-mean condition in the tropical Pacific Ocean. To establish

such a realistic mean condition in the coupled model, we first force the model with a surface heat flux of the form of $Q = -\partial_t Q (T - T_m)$, where $\partial_t Q$ is a damping coefficient and T_m is the observed annual-mean SST in the tropical Pacific Ocean. The damping coefficient $\partial_t Q$ is intentionally assigned an unrealistically large value of 15 000 W m^{-2} so that the model mixed layer temperature quickly relaxes back to the observed annual-mean SST. The model SST then forces the atmospheric component to generate steady surface winds, which in turn produce mean surface currents and a mean structure of thermocline in the ocean model. After five years of integration, the coupled model essentially reaches an equilibrium. As shown in Fig. 12a, the mean fields produced by the coupled model bear a close resemblance to the observed fields. Upon obtaining the mean fields, a weak antisymmetric anomaly, which has its maximum value along the eastern boundary and which attenuates westward, is introduced to the mean temperature field. Hence, the initial temperature is

$$T(x, y, 0) = T_0(x, y) + 0.5°C \tanh(y/L_y)$$

$$\times \exp\{-[(x - x_e)/L_x]^2\},$$

where T_0 is the mean temperature produced by the coupled model, x_e is the location of the model eastern boundary, and $L_x = 1000$ km is the zonal e-folding scale of the disturbance. The model is then integrated for another 200 days with a fixed surface heat flux given by $Q = -\partial_t Q (T_0 - T_m)$ plus a Newtonian damping term $-\epsilon (T - T_m)$ with $\epsilon = 1/150$ day^{-1}. Throughout the experiment, the subsurface temperature $\bar{T}_{sub}$ and its derivative $\partial_z \bar{T}_{sub}$ in the model are chosen to be the observed annual-mean values at 50 m.

Figure 12 displays "snapshots" of the model SST and winds in the eastern Pacific at times $t = 0, 40, 80, 120, 160,$ and 200 days. The development of the cold tongue in the model is clearly revealed. The initial growth of the temperature anomaly first occurs just south of the equator near the eastern boundary. As the disturbance grows further, it begins to propagate westward with the coldest temperature in the south of the equator. Figure 13 depicts the time evolution of the temperature and wind anomalies along 90°W and along the equator. As can be seen, the SST anomaly is asymmetric about the equator with strong cooling developed in the Southern Hemisphere. The corresponding southerly wind, on the other hand, appears to the north of the equator. This structure of the SST and meridional wind is similar to the one observed in the eastern equatorial Pacific and Atlantic Oceans during the onset of cold tongues (Mitchell and Wallace 1992). The westward propagation of the SST anomalies along the equator is also evident (Figs. 13c,d). The estimated phase speed is approximately 40 cm s^{-1}, similar to the observed value. Using the linear regression method, we estimate that the e-folding timescale for growth of the coupled instability is about 60 days, which is longer
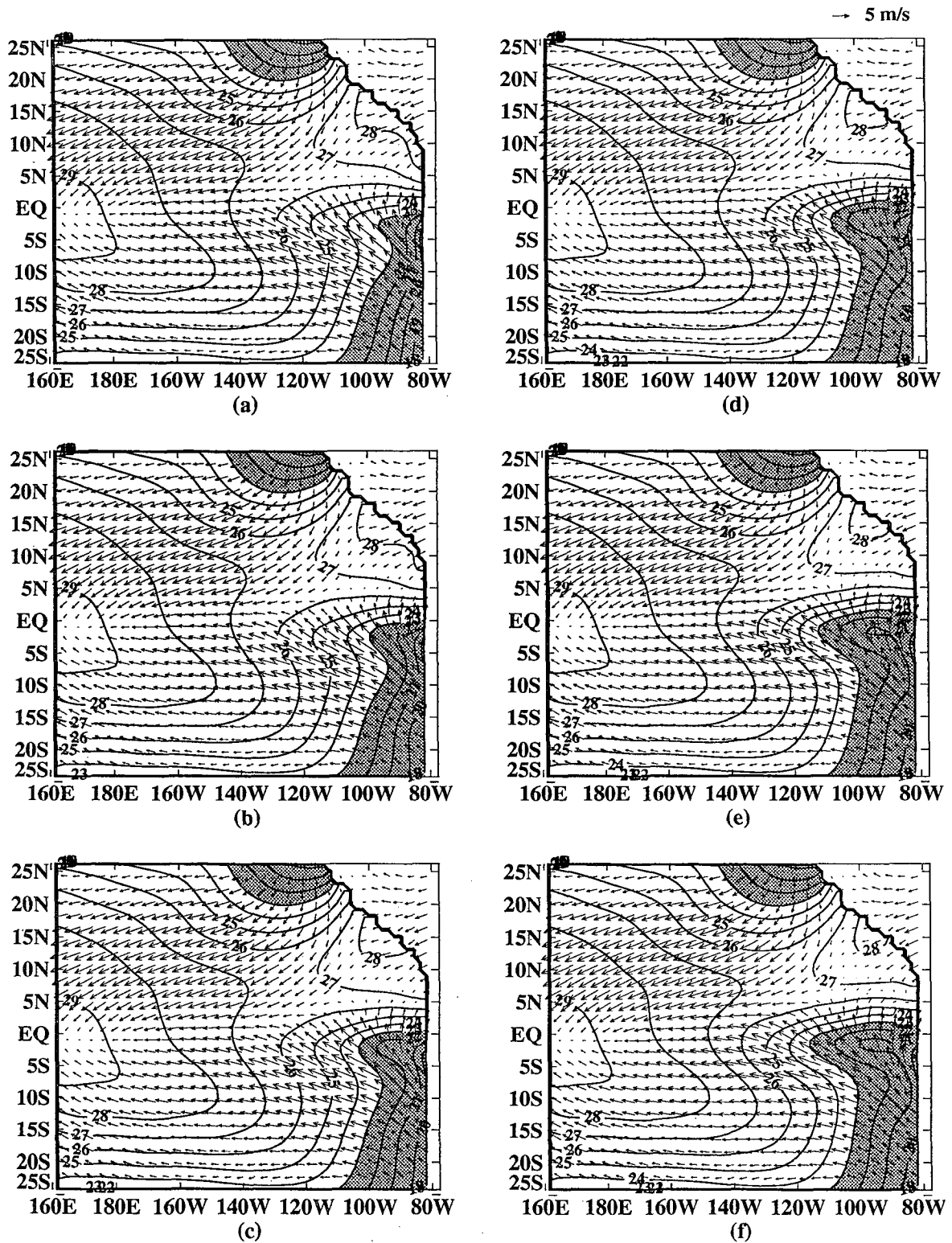
FIG. 12. Snapshots of the model SST and surface wind stresses in the eastern tropical Pacific at (a) $t = 0$, (b) $t = 40$, (c) $t = 80$, (d) $t = 120$, (e) $t = 160$, and (f) $t = 200$ (days). The mean conditions of the coupled model resemble closely the observed annual-mean conditions in the eastern Pacific. The scaling vector on the upper right corner represents a surface wind velocity of 5 m s^{-1}. Contour intervals are 1°C in all the figures.
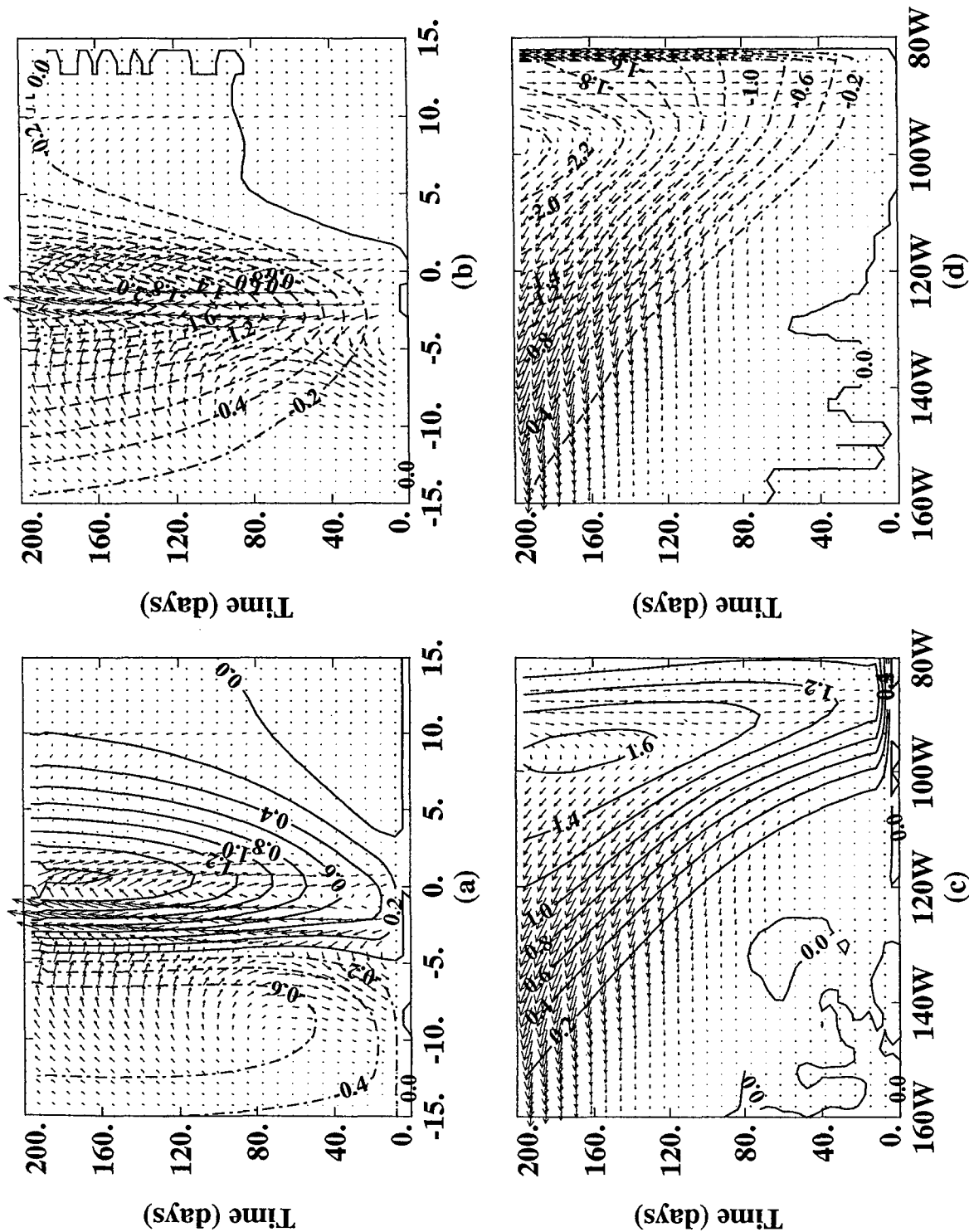
FIG. 13. Time–latitude plots of (a) meridional wind anomaly and (b) model SST anomaly along 90°W taken from the experiment with realistic mean condition. (c) and (d) show the time–longitude plots of zonal wind stress and SST along the equator. As in Fig. 10, vectors illustrate the effects of the Ekman up/downwelling and the surface Ekman drifts. Contour intervals are 0.2°C in (b) and (d) and 0.2 dyn cm^{-2} in (a) and (c).
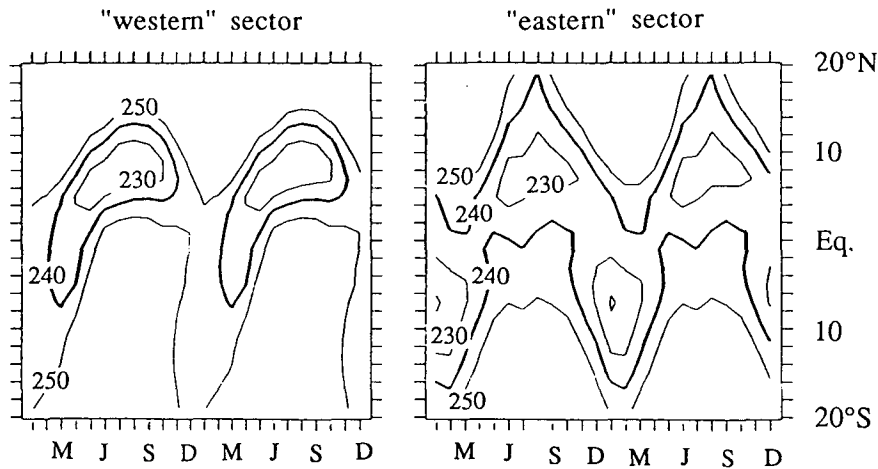
FIG. 14. Latitude–time plot of zonal-mean outgoing longwave radiation (OLR) for (a) the "western" sector, which includes the eastern Pacific Ocean (140°W), South America, the Atlantic Ocean, and Africa (40°E), and (b) the "eastern" sector, which includes the Indian Ocean (40°E), Indonesia, and the western and central Pacific Ocean (140°W). Contour interval is 10 W m^{-2}. (from Mitchell and Wallace 1992).

than the value in the idealized case. The reduction in growth rate is probably due to the presence of the mean equatorial upwelling induced by the mean surface winds, which acts like a Newtonian damping to the SST anomaly.

Additional coupled runs have also been conducted to examine what happens if the sign of initial SST anomaly is reversed. The results show that, unless the initial anomaly is of large amplitude, the disturbance will decay with time. However, for a sufficiently cold SST anomaly in the Northern Hemisphere, the cold tongue can form in the north of the equator. This is because the mean surface wind stresses are asymmetric about the equator with a strong convergence in the north, so that they produce a strong Ekman downwelling to the north of equator. Therefore, unless the initial SST gradient is large enough to generate sufficiently strong Ekman upwelling to overcome the mean downwelling in the region, it cannot initiate the positive feedback process and generate coupled instability. This result implies that given the asymmetry of the mean state, strong seasonal variations of SST are likely to occur in the cold tongue regions.

5. Conclusion and discussion

In the western tropical Pacific the seasonal north–south movements of the convective zones are in response to seasonal changes in sea surface temperature. In that region, where the thermocline is deep, sea surface temperature changes depend primarily on the local flux of heat across the ocean surface, and the convective zones, which are over the warmest waters, essentially "follow" the sun back and forth across the equator. Conditions are symmetrical about the equator so

that a semiannual signal is dominant at the equator. This is evident in Fig. 14 in which it is also clear that matters are very different in the eastern tropical Pacific and Atlantic. In the latter regions where the thermocline is shallow, sea surface temperatures depend on heat fluxes and on the dynamical response of the ocean to the winds. The winds in turn depend on sea surface temperature changes. In other words, interactions between the ocean and atmosphere come into play. This paper investigated the coupled ocean–atmosphere modes that may play a large role in the seasonal cycle—namely, those that are antisymmetrical about the equator. Our analyses indicate that the processes of crucial importance to these modes are the divergence of surface currents and the associated upwelling that alters sea surface temperatures. These modes therefore have a shallow vertical structure and require the mean depth of the thermocline to be small—that is why they are absent from the western tropical Pacific. They are very different from the coupled ocean–atmosphere modes involved in El Niño because those are associated with a large-scale horizontal redistribution of heat and with vertical movements of the thermocline. The modes discussed here do not involve significant vertical movements of the thermocline. They depend on feedbacks in which southerly winds induce upwelling and low sea surface temperatures to the south of the equator. The resultant meridional sea surface temperature gradients reinforce the winds, which in turn amplify the temperature gradients. The most unstable modes have zero zonal wavenumber and zero frequency. This result has interesting implications. First of all, the modes affect the earth's response to the time-mean solar radiation. Even though that forcing is symmetrical about the equator, the response is unlikely to be symmetrical be-

SURFACE TEMPERATURE   EQ

TIME (months)

D

O

A

J

A

F

40°E   120°E   160°W   80°W   0°

ZONAL WIND   EQ

TIME (months)

D

O

A

J

A

F

40°E   120°E   160°W   80°W   0°

MERIDIONAL WIND   ı   EQ

TIME (months)

D

O

A

J

A

F

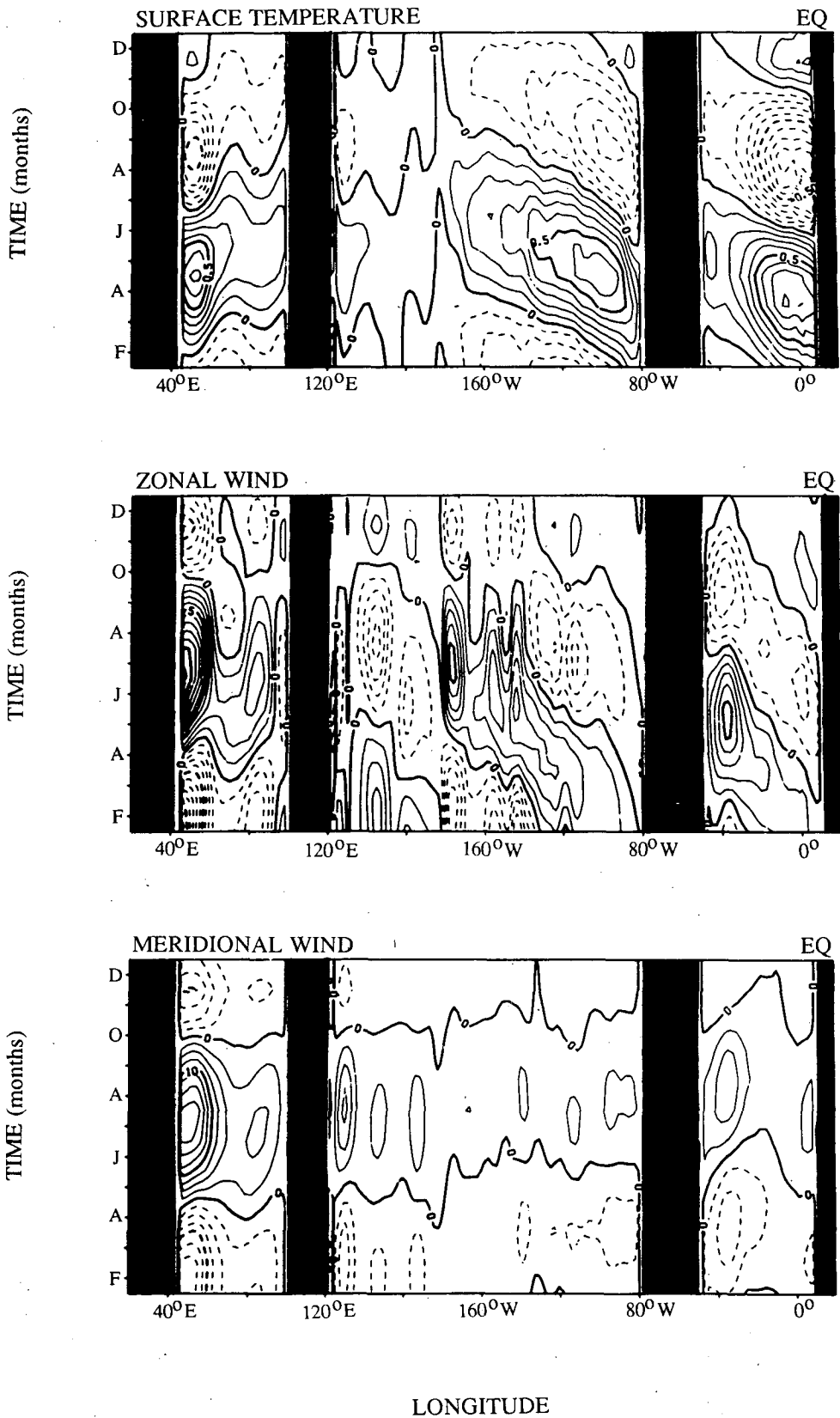40°E   120°E   160°W   80°W   0°

LONGITUDE

FIG. 15. Time–longitude plot of (a) the observed sea surface temperature, (b) the observed zonal component of surface winds, and (c) the observed meridional component of surface winds along the equator. Contour intervals are 0.5°C in (a) and 0.5 m s^{-1} in (b) and (c).

a)   APRIL   → 10 m s^{-1}

b)   OCTOBER

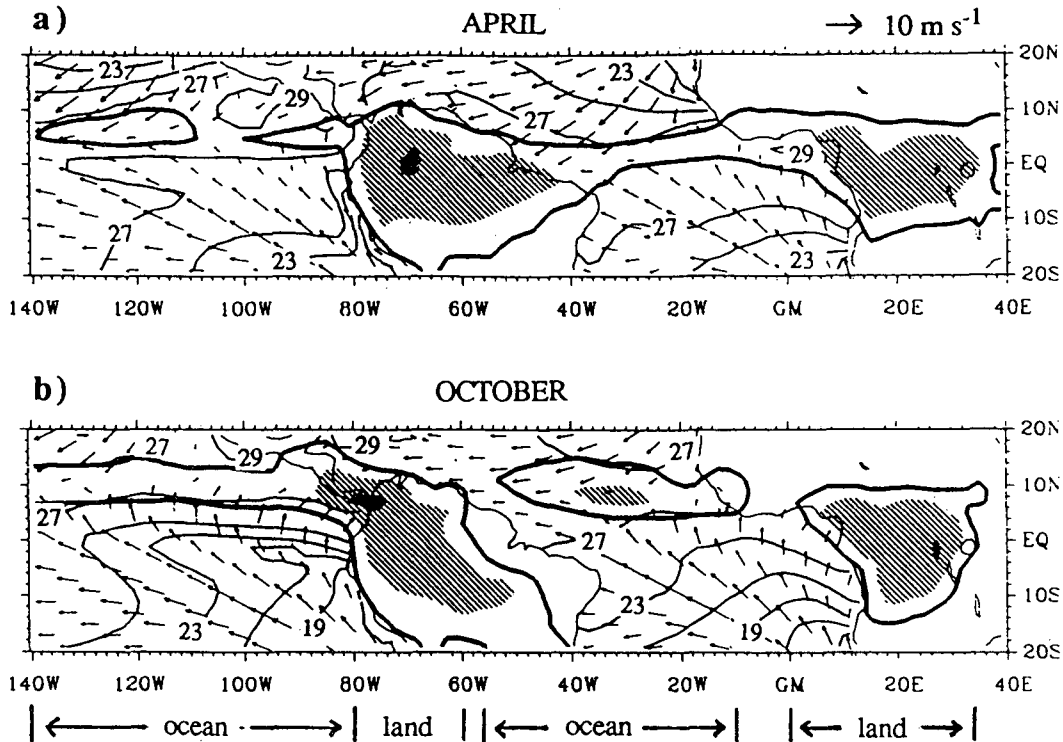|← ocean ——→ | land | |← ocean ——→| |← land →|

FIG. 16. Map of OLR, vector surface wind, and SST in the "Western" sector defined in Fig. 14 for (a) April and (b) October. The heavy contour denotes OLR values of 240 W m^{-2}, and shading (dark) indicates OLR values between 220 and 200 W m^{-2} (<200 W m^{-2}). The SST contour interval is 2°C. Surface winds with wind speed <1 m s^{-1} are not plotted (from Mitchell and Wallace 1992).

cause these modes amplify any perturbation to create asymmetrical conditions. In our numerical experiments that explore this phenomenon the atmospheric convective zones and maximum sea surface temperatures can ultimately be in either hemisphere. In reality they are found to the north of the equator. We intend, in subsequent studies, to explore the factors that favor the Northern Hemisphere—factors such as the configuration of the coastlines.

The coupled ocean–atmosphere modes with zero frequency also affect the earth's response to seasonal variations in solar radiation. Figure 15 shows that response as a function of time and longitude along the equator. The sea surface temperature and zonal wind component are seen to have westward phase propagation—a feature noted by Horel (1982), Chao and Philander (1993), and Chang (1994). This, the symmetric part of the response, is discussed toward the end of section 3 of this paper. In Fig. 15 the antisymmetric part of the response, as revealed by the meridional component of the wind, has no zonal phase propagation, and the zonal wavenumber in the Pacific is clearly zero. In other words, whereas the symmetrical part of the response involves an air–sea mode with a period of one year and the corresponding nonzero zonal wavenumber, the antisymmetric part of the response is dif-

ferent. It involves air–sea modes with zero zonal wavenumber and, as is evident in Fig. 15, with a complex time dependence, not simply an annual harmonic. This antisymmetric response can easily be explained in terms of the zero frequency, zero zonal wavenumber mode, which has a rapid growth rate. Consider conditions toward the end of the northern summer. At that time, sea surface temperatures to the south of the equator in the eastern tropical Pacific are low for two reasons: 1) solar radiation has been low for several months and 2) southerly winds that converge onto the ITCZ north of the equator have contributed to low sea surface temperatures by inducing upwelling. The latter process involves the coupled ocean–atmosphere modes because the southerly winds are intensified by the surface temperature gradients they create. The relevant modes are those with zero frequency and zonal wavenumber. Now as the sun proceeds to "move" southward, its "attempts" to heat the surface waters south of the equator are countered by the ocean–atmosphere interactions that "try" to keep those waters cool. The ITCZ over the eastern Pacific and Atlantic therefore remains over the warmest waters north of the equator. Over the adjacent landmasses matters are very different because there are no ocean–atmosphere interactions to oppose heating by the sun. The convective zones over the con-

tinents of Africa and South America therefore move far southward, while those over the oceans remain in northerly positions. This separation of the oceanic from the continental convective zones is strikingly evident in Fig. 16 from Mitchell and Wallace (1992). It is only toward the very end of the southern summer, in March, that solar radiation warms the waters south of the equator sufficiently for the ITCZ to move close to the equator. When the sun next "returns" to the north, both the reduction in solar radiation and ocean–atmosphere interactions cool the region south of the equator very rapidly. Once again the mode with zero frequency and zonal wavenumber comes into play. The result is the highly nonsinusoidal response of Fig. 14 to the sinusoidal variation in solar radiation. If the mean state were symmetrical relative to the equator then one would expect a nonsinusoidal response in which the ITCZ moves jerkily back and forth across the equator. Because of the asymmetry of the mean state the region north of the equator never becomes cold and the ITCZ never leaves the Northern Hemisphere entirely. The result, shown in Fig. 14, is the response with an annual cycle on the equator even when the annual cycle of the forcing function, the solar radiation, vanishes at the equator.

The seasonal cycle involves symmetrical and antisymmetrical coupled ocean–atmosphere modes. In our numerical experiments such modes come into play when we specify a realistic mean state that is asymmetrical about the equator. Earlier we speculated that the geometries of coastlines could contribute to the asymmetry. Those geometries could also affect the ocean–atmosphere modes. In particular, the coastal geometries of the eastern Pacific and Atlantic Oceans parallel the southeast trades in the Southern Hemisphere, which tends to promote coastal upwelling along the coasts of South America and Africa. The upwelling brings cold water to the surface, increasing the offshore temperature gradient along the coast. The intensifying temperature gradient enhances the alongshore component of surface wind stress, which promotes further upwelling along the coast. This positive feedback between atmosphere and ocean presumably will lead to another coupled unstable mode in the coastal region. The coastal mode and the equatorial modes are ultimately connected. At the moment, it is not clear how these two modes are related. This problem is now under investigation.

APPENDIX

Governing Equations of the Coupled Model

The governing equations for the atmosphere are as follows (see Wang and Li 1993):

$$\frac{\partial \mathbf{V}}{\partial t} + \beta y \mathbf{k} \times \mathbf{V} = -\nabla \Phi - \epsilon \mathbf{V} \qquad (A1)$$

$$\frac{\partial \Phi}{\partial t} + C_a^2 (1 - \delta I)\nabla \cdot \mathbf{V} = -\mu \Phi - \mu G(T_s - \bar{T}_s)$$
$$- C_a^2 d(1 - \delta B)\nabla \cdot \mathbf{V}_B - \delta F |V_s|(T_s - T^*) \quad (A2)$$

$$\beta y \mathbf{k} \times \mathbf{V}_B = -\nabla \Phi + A\nabla T_s - E\mathbf{V}_B, \qquad (A3)$$

where $\bar{T}_s$ is the domain-averaged SST; ϵ is the Rayleigh friction coefficient in the free-tropospheric layer; μ is Newtonian cooling coefficient; $|V_s|$ the total surface wind speed, which has a minimum value of 4 m s^{-1}; and δ is a switch-on parameter for nonlinear heating. The nondimensional parameters in Eqs. (A1)–(A3) are

$$I = \frac{4RL_c b(\bar{q}_3 - \bar{q}_1)}{C_p S_2 (p_e^2 - p_u^2)} \quad \text{condensational}$$

     heating coefficient in the free troposphere

$$B = \frac{4RL_c b \bar{q}_e}{C_p S_2 (p_e^2 - p_u^2)} \quad \text{condensational}$$

     heating coefficient in the boundary layer

$$G = \frac{p_e - p_u}{2(p_e + p_u)}$$

     coefficient of longwave radiational forcing

$$d = \frac{2(p_s - p_e)}{p_e - p_u} \quad \text{depth of boundary layer}$$

$$F = \left(\frac{C_a}{\beta}\right)^{1/2} \frac{\rho_s g L_c b}{C_p(p_e + p_u)} C_E K_q$$

     coefficient of evaporation forcing

$$A = \frac{p_s - p_e}{2p_e} \quad \text{coefficient of SST gradient forcing}$$

$$E = \frac{\rho_s g K_D}{(p_s - p_e)\sqrt{\beta C_a}}$$

     Ekman number of the boundary layer.

In the above equations, the mean specific humidity at the upper troposphere $\bar{q}_1$ is set to be 4×10^{-4}, and the specific humidity in the boundary layer $\bar{q}_e$ and upper free-tropospheric layers $\bar{q}_3$ are given by

TABLE A1. The atmospheric model parameters:

Symbol	Parameter	Value
ϵ	Rayleigh friction coefficient	1×10^{-5} s^{-1}
C_a	Gravity wave speed	48 m s^{-1}
δ	Switch-on parameter for nonlinear heating	1.0 (linear heating)
μ	Newtonian cooling coefficient	1×10^{-5} s^{-1}
R	Gas constant of air	289 m^2 s^{-2} k^{-1}
L_c	Latent heat coefficient	2.5×10^6 m^2 s^{-2}
b	Efficiency of condensation	0.75
p_e	Pressure at the top of boundary layer	85 kPa
p_s	Surface pressure	100 kPa
p_u	Pressure at the top of the free atmosphere	10 kPa
H	Density scale height	7.8 km
H_1	Water vapor density scale height	2.2 km
ρ_s	Air density in the boundary layer	1.22 kg m^{-1}
S_2	Static stability in the troposphere	3.324×10^{-6} m^2 s^{-2} Pa^{-2}
r	Ratio of the equilibrium temperature deviation at the mid-troposphere to SST deviation	0.6
C_E	Coefficient of turbulent vertical moisture flux	1.5×10^{-3}
K_D	Surface friction coefficient	2.3×10^{-2}m s^{-1}
K_q	Evaporational heating coefficient	6.95×10^{-4} K^{-1}
T^*	Reference temperature	293.2 K^{-1}

$$\bar{q}_e = q_0 \frac{(p_s/p_0)^m - (p_e/p_0)^m}{m(p_s - p_e)} \quad \text{and}$$

$$\bar{q}_3 = q_0 \frac{(p_e/p_0)^m - (p_e/p_2)^m}{m(p_e - p_2)},$$

where q_0 represents specific humidity at the surface as a function of SST T_s(K); $q_0 = 10^{-3}[18. + 0.67$ K$^{-1}(T_s - 300$ K$)]$; $p_0 = 100$ kPa; and $m = H/H_1$ is the ratio of the density scale height H to the water vapor density scale height H_1. The other basic model parameters used in the coupled model experiments are listed in Table A1.

The governing equations for the ocean are (see Seager et al. 1988; Chang 1994)

$$\frac{\partial \mathbf{u}}{\partial t} + f \mathbf{k} \times \mathbf{u} = g'\nabla h + \frac{\tau}{H} + \nu\nabla^2\mathbf{u} \quad \text{(A4)}$$

$$\left(\frac{\partial h}{\partial t}\right) + H\nabla\cdot\mathbf{u} = \nu\nabla^2 h \quad \text{(A5)}$$

$$\frac{\partial T}{\partial t} + \mathbf{u}_s\cdot\nabla T = \frac{Q}{\rho_0 C_p H_s} + \kappa\nabla^2 T$$

$$- \frac{1}{H_s} w_e H(w_e)(T - T_e), \quad \text{(A6)}$$

where the horizontal velocity in the surface mixed layer $\mathbf{u}_s$ is determined from the surface Ekman flow $\mathbf{u}_e$ and the velocity $\mathbf{u}$ given by dynamic equations (A4):

$$\mathbf{u}_s = \mathbf{u} + \mathbf{u}_e(H - H_s)/H;$$

the Ekman flow $\mathbf{u}_e$ is given by

$$r_s u_e - f v_e = \tau_x/H_s, \quad r_s v_e + f u_e = \tau_y/H_s.$$

The entrainment velocity w_e is determined as divergence of the surface velocity; that is,

$$w_e = H_s \nabla\cdot\mathbf{u}_s.$$

The temperature of entrained water beneath the base of the mixed layer T_e is given by $T_e = (1 - \gamma)T + \gamma T_d$, where γ is an adjustable parameter taken to be 0.75 and T_d is the temperature immediately beneath the base of the mixed layer. Since the model does not predict the change of subsurface T_d, changes in T_d are assumed to be related to the changes in the model layer depth. In this study, we use a simple linear relation given by Eq. (13). The model parameters used in the coupled model experiments are listed in Table A2.

TABLE A2. Oceanic model parameters.

Symbol	Parameter	Value
g'	Reduced gravity	0.056 m s^{-2}
H_S	Depth of surface mixed layer	50 m
H	Depth of thermocline	150 m
ν	Eddy viscosity	5×10^3 m^2 s
κ	Eddy diffusivity	10^3 m^2 s

REFERENCES

Battisit, D. S., and A. C. Hirst, 1989: Interannual variability in the tropical atmosphere–ocean system: Influence of the basic state and ocean geometry. J. Atmos. Sci., 45, 1687–1712.

Cane, M. A., 1979: The response of an equatorial ocean to simple wind-stress patterns. I. Model formulation and analytic results. J. Mar. Res., 37, 233–252.

——, S. C. Dolan, and S. E. Zebiak, 1986: Experimental forecasts of the 1982/83 El Niño. Nature, 321, 827–832.

Chang, P., 1993: Seasonal cycle of sea surface temperature and mixed layer heat budget in the tropical oceans. Geophys. Res. Lett., 20, 2079–2082.

——, 1994: A study of seasonal cycle of sea surface temperature in the tropical Pacific ocean using reduced gravity models. *J. Geophys. Res.,* **99,** 7725–7742.

Chao, Y., and G. Philander, 1993: The structure of the Southern Oscillation. *J. Climate,* **6,** 450–469.

Hayes, S. P., P. Chang, and M. J. McPhaden, 1991: Variability of the sea surface temperature in the eastern equatorial Pacific during 1986–1988. *J. Geophys. Res.,* **96,** 10 553–10 566.

Hirst, A. C., 1986: Unstable and damped equatorial modes in simple coupled ocean–atmosphere models. *J. Atmos. Sci.,* **43,** 606–630.

Horel, J. D., 1982: The annual cycle in the tropical Pacific atmosphere and ocean. *Mon. Wea. Rev.,* **110,** 1863–1878.

Koeberle, C., and S. G. H. Philander, 1994: On the processes that control seasonal variations of sea surface temperatures in the tropical Pacific ocean. *Tellus,* **46A,** 481–496.

Lindzen, R. S., and S. Nigam, 1987: On the role of sea surface temperature gradients in forcing low level winds and convergence in the tropics. *J. Atmos. Sci.,* **44,** 2240–2458.

Mitchell, T. P., and J. M. Wallace, 1992: On the annual cycle in equatorial convection and sea-surface temperature. *J. Climate,* **5,** 1140–1156.

Neelin, J. D., 1989: On the interpretation of the Gill model. *J. Atmos. Sci.,* **46,** 2466–2468.

——, 1991: The slow sea surface temperature mode and the fast-wave limit: Analytic theory for tropical interannual oscillations and experiments in a hybrid coupled model. *J. Atmos. Sci.,* **48,** 584–606.

Seager, R., S. E. Zebiak, and M. A. Cane, 1988: A model of the tropical Pacific sea surface temperature climatology. *J. Geophys. Res.,* **93**(C2), 1265–1280.

Suarez, M. J., and P. S. Schopf, 1988: A delayed oscillator for ENSO. *J. Atmos. Sci.,* **45,** 3283–3287.

Wang, B., 1994: On the annual cycle in the equatorial Pacific cold tongue. *J. Climate,* submitted.

——, and T. Li, 1993: A simple tropical atmosphere model of relevance to short-term climate variations. Part I: Model physics. *J. Atmos. Sci.,* **50,** 260–284.

Zebiak, S. E., and M. A. Cane, 1987: A model ENSO. *Mon. Wea. Rev.,* **115,** 2262–2278.